

See discussions, stats, and author profiles for this publication at: <https://www.researchgate.net/publication/46819128>

# Polarized X-ray Absorption Near-Edge Structure Spectroscopy of Neuroglobin and Myoglobin Single Crystals

ARTICLE in THE JOURNAL OF PHYSICAL CHEMISTRY B · SEPTEMBER 2010

Impact Factor: 3.3 · DOI: 10.1021/jp104395g · Source: PubMed

CITATIONS

10

READS

21

6 AUTHORS, INCLUDING:



**Alessandro Arcovito**

Catholic University of the Sacred Heart

70 PUBLICATIONS 1,052 CITATIONS

SEE PROFILE



**Michele Cianci**

European Molecular Biology Laboratory

60 PUBLICATIONS 721 CITATIONS

SEE PROFILE



**Beatrice Vallone**

Sapienza University of Rome

91 PUBLICATIONS 2,614 CITATIONS

SEE PROFILE



**Stefano della longa**

Università degli Studi dell'Aquila

115 PUBLICATIONS 2,013 CITATIONS

SEE PROFILE

# Polarized X-ray Absorption Near-Edge Structure Spectroscopy of Neuroglobin and Myoglobin Single Crystals

Alessandro Arcovito,<sup>\*,†</sup> Chiara Ardiccioni,<sup>‡</sup> Michele Cianci,<sup>§</sup> Paola D'Angelo,<sup>||</sup> Beatrice Vallone,<sup>‡</sup> and Stefano Della Longa<sup>\*,⊥</sup>

*Istituto di Biochimica e Biochimica Clinica, Università Cattolica del Sacro Cuore, L. go F. Vito 1, 00168 Rome, Italy, Dipartimento di Scienze Biochimiche "A. Rossi-Fanelli", Sapienza Università di Roma, Piazzale A. Moro 5, 00185 Rome, Italy, European Molecular Biology Laboratory, Hamburg Outstation, Notkestrasse 85, 22603, Hamburg, Germany, Dipartimento di Chimica, Sapienza Università di Roma, Piazzale A. Moro 5, 00185 Rome, Italy, and Dipartimento di Medicina Sperimentale, Università "L'Aquila", Via Vetoio, 67100 L'Aquila, Italy*

Received: May 14, 2010; Revised Manuscript Received: September 6, 2010

Polarized Fe K-edge X-ray absorption near-edge structure (XANES) spectra of murine carbonmonoxy–neuroglobin (NgbCO) single crystals have been collected and compared with a number of derivatives of sperm whale myoglobin (Mb), that is, the nitrosyl (MbNO) and deoxy (Mb) derivatives, the previously reported cyanomet (MbCN) and carbonmonoxy (MbCO) derivatives, and the cryogenic photoproduct of MbCO (Mb•CO). The single crystals under study exhibit a strong XANES angular dichroism which allows the heme geometry of each sample to be analyzed with extremely high accuracy via the full multiple scattering (MS) approach. The results of two alternative methods to undergo the MS analysis have been compared with high resolution X-ray diffraction (XRD) data and with X-ray absorption spectroscopy (XAS) data in solution. As a result of the present analysis, the Fe-heme structure in solution and in the cryo-trapped NgbCO single crystal (which cracks at room temperature) are the same. Accordingly, the residual energy involved in the protein relaxation responsible of crystal cracking at room temperature after CO binding does not reside in the heme pocket. A combined approach (polarized XANES and XRD) is suggested to be applied on the same single crystals of metalloproteins at opportunely equipped synchrotron beamlines.

## Introduction

Biochemical reactions taking place in the living cell demand these reactions to be highly specific. Proteins achieve such specificity through geometrical and chemical precision in molecular interactions. As a consequence, a detailed determination of protein structure, especially at the level of the active site, is a critical step in structural biology research.<sup>1</sup>

X-ray absorption spectroscopy (XAS) is a powerful technique able to investigate both local structure and dynamics of protein metal centers<sup>2,3</sup> and especially on a wide class of them such as hemeproteins.<sup>4–8</sup> In fact, XAS can reveal structural parameters around metal centers with very high accuracy, comparable to that of small-molecule crystallography, typically around 1 Å resolution. Such detailed structural data can be essential for elucidating the function of the hemeprotein under study,<sup>9</sup> as structural changes to the metal coordination during redox or substrate-binding reactions are generally <0.1 Å and hence remain unnoticed in standard protein crystallography at lower resolution.

Moreover, even when the X-ray structure of a protein expressed in the cell during a relevant physiological process is

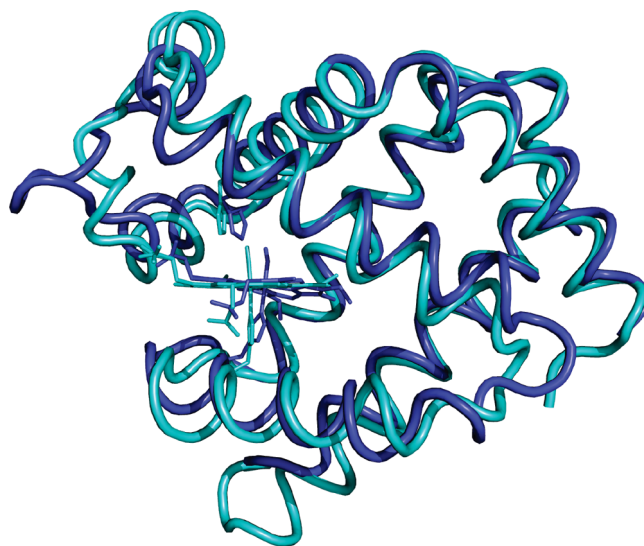


**Figure 1.** Structural superimposition of murine NgbCO (blue) and sperm whale MbCO (light blue), based on the position of the backbone C $\alpha$  atoms.

known, this knowledge is sometimes not enough to unravel its function. For instance, Figure 1 shows the noticeable superimposition of the three-dimensional structure of two hemeproteins belonging to globin family, myoglobin (MbCO; PDB code: 1A6G) and neuroglobin (NgbCO; PDB code: 1W92); the former one is abundant in the muscles, while the latter is found in the nervous system of vertebrates. Both of these proteins can bind

\* Corresponding authors. E-mail: alessandro.arcovito@rm.unicatt.it; tel.: +39 06 30156706; fax: +39 06 30156783 (A.A.). E-mail: dlunga@caspur.it; tel.: +39 0862 433568; fax: +39 0862 433523 (S.D.L.).

<sup>†</sup> Università Cattolica del Sacro Cuore.

<sup>‡</sup> Dipartimento di Scienze Biochimiche "A. Rossi-Fanelli", Sapienza Università di Roma.

<sup>§</sup> European Molecular Biology Laboratory.

<sup>||</sup> Dipartimento di Chimica, Sapienza Università di Roma.

<sup>⊥</sup> Università "L'Aquila".

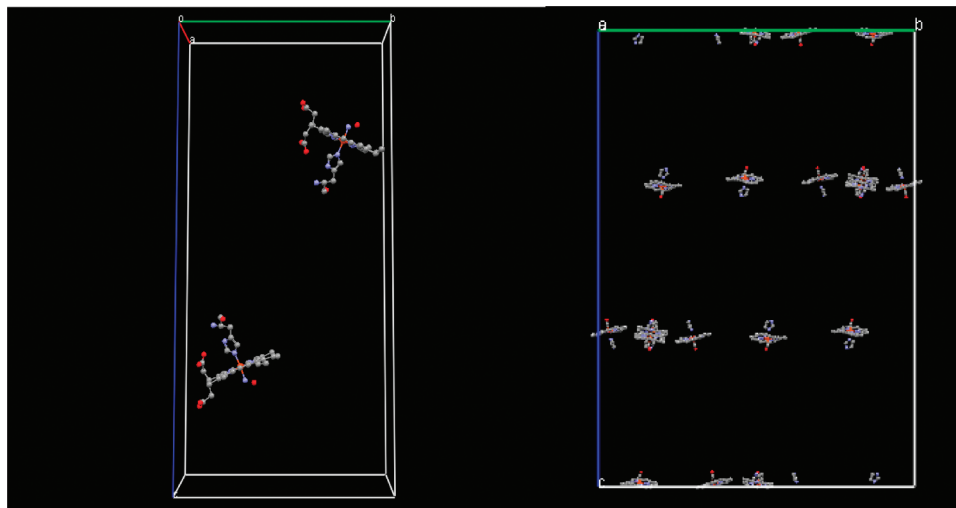


**Figure 2.** Sketches of the 2 oriented hemes of MbNO (on the left,  $P2_1$  space group) and the 18 hemes of murine NgbCO (on the right,  $R32$  space group) in their crystal unit cells.

oxygen and diatomic gases reversibly and have strong similarities in the fold, but the Fe-heme properties are quite different: the 5-coordinate species in Ngb is only a transient state, and its sixth ligand position in the absence of an exogenous ligand is always occupied by an endogenous histidine. Whereas Mb is a well-known protein involved in oxygen storage and delivery in muscles as well as in the cell detoxification process,<sup>10</sup> this function in Ngb is ruled out, and its role in the cell is still under debate.<sup>11,12</sup>

X-ray absorption near-edge structure (XANES) fingerprints are usually interpreted to elucidate the oxidation state and the overall symmetry of the metal site by direct comparison with model standards.<sup>13</sup> Furthermore, in many cases, for hemeproteins, the XANES dichroism of the heme can be exploited. In the general case, assuming that the incident beam is linearly polarized along a direction denoted by the vector  $\epsilon$ , each spectrum  $j$  (i.e., each crystal orientation) samples a particular direction  $\epsilon_j$ . The fluorescence intensity emitted as a function of the energy  $E$  from a small crystal is proportional, within the dipole approximation of the photoelectron absorption cross section, to the quadratic form  $\sigma_j$

$$\sigma_j(E) = \epsilon_j^T \sigma(E) \epsilon_j \quad (1)$$

where  $\sigma(E)$  denotes the absorption tensor, the superscript  $T$  indicates the transpose, and  $\sigma_j(E)$  denotes the effective scalar linear absorption coefficient along the direction  $\epsilon_j$ . According to the crystal symmetry, the absorption tensor is provided by a certain number of orientation-dependent spectra, and the “solution equivalent spectrum”, comparable with the solution spectrum, is obtained by the trace of the tensor, divided by three.<sup>14</sup>

When the local structure around a metal center has a  $C_4$  symmetry (approximately the one of the Fe-heme site), a simplified approach can be adopted. First, it is advantageous to consider the XAS components linearly polarized along its symmetry axis (the heme normal),  $I_{\text{normal}}$ , and along a direction in the  $C_4$  plane (the heme plane),  $I_{\text{heme}}$ . Assuming perfect  $C_4$  symmetry, for a certain angle  $\vartheta$  between the polarization vector  $\epsilon$  and the heme normal, the polarized spectrum is given, as a function of  $I_{\text{heme}}$  and  $I_{\text{normal}}$ , simply by

$$I_\vartheta = I_{\text{normal}} \cos^2 \vartheta + I_{\text{heme}} \sin^2 \vartheta \quad (2)$$

that means that the X-ray absorption cross section of the heme is approximately dichroic; in the presence of  $m$  symmetry related hemes in the unit cell of the crystal it is possible to write:

$$\begin{aligned} I_\vartheta &= \frac{1}{m} \sum_1^m (I_{\text{normal}} \cos^2 n_i \vartheta + I_{\text{heme}} \sin^2 n_i \vartheta) \\ &= \frac{1}{m} [I_{\text{normal}} \sum_1^m (\cos^2 n_i \vartheta) + I_{\text{heme}} \sum_1^m (1 - \cos^2 n_i \vartheta)] \\ &= a_\vartheta I_{\text{normal}} + b_\vartheta I_{\text{heme}} \end{aligned} \quad (3)$$

where  $a_\vartheta = (1/m) \sum_1^m (\cos^2 n_i \vartheta)$ ;  $b_\vartheta = 1 - a_\vartheta$ ;  $\vartheta$  is now a rotational angle of an oriented crystal in the laboratory system, and  $n_i \vartheta$  are the angles between each heme normal  $n_i$  and the X-ray polarization vector  $\epsilon$  that correspond to  $\vartheta$ . By increasing the  $m$  value, and if the directions of the several heme normal vectors are homogeneously scattered on the rotational sphere, the collected XAS signal approaches the average solution signal. The value  $a_\vartheta = 0.33$  (corresponding for a single heme normal to the “magic angle”  $n_i \vartheta = 54.7^\circ$ ) gives the 1:2 ratio between  $I_{\text{normal}}$  and  $I_{\text{heme}}$ . In these conditions, and under the approximations stated above, the polarized XAS spectrum collected on the single crystal is directly superimposable to the XAS spectrum collected in solution, residual small differences depending on experimental conditions and on the degree of departure from a perfect  $C_4$  symmetry. On the contrary, the more the  $m$  symmetry-related heme planes are oriented parallel (or antiparallel) in the unit cell, the more the XAS dichroism is maintained in the single crystal; in all of these cases, the XAS angular dependence can provide an enhanced resolution of the heme site with respect to both X-ray crystallography and solution XAS.

One example of strong dichroism is the  $P2_1$  space group of sperm whale myoglobin having two hemes in the unit cell oriented almost (anti)parallel at  $23^\circ$  from the heme normals. Figure 2, left frame, shows the two hemes on projections along the crystal axes, in the case of carbonmonoxy-derivative (Protein Data Bank, PDB, code 1A6G). It is possible to calculate the  $a_\vartheta$  coefficient for any chosen orientation from the PDB data entry. For example, by rotating the crystal around the  $b$ -axis, kept perpendicular to the X-ray polarization vector  $\epsilon$  (in a synchrotron radiation experiment the  $\epsilon$  vector is in the plane of the electron

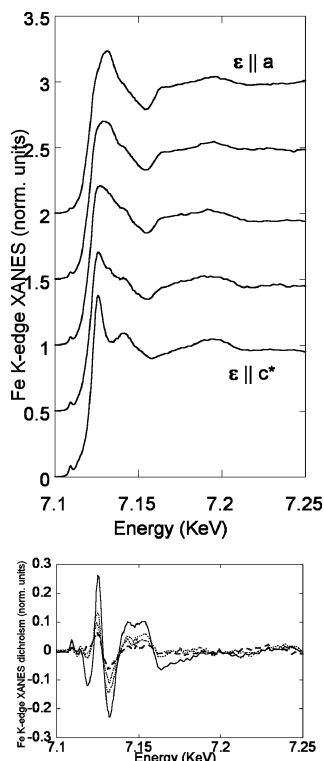


**Figure 3.** Angular dependence of the Fe K-edge polarized XANES spectra of MbCN. By rotating the crystal around the **b** crystal axis, from bottom ( $\epsilon || c^*$ ) to top ( $\epsilon || a$ ), the angle between each heme normal and the  $\epsilon$  vector is  $23^\circ$ ,  $45^\circ$ ,  $56^\circ$ ,  $65^\circ$ , and  $90^\circ$ , respectively. The dichroism of the XANES signal is revealed by observing the same difference XANES spectrum with increasing intensity as increases the angular variation (lower frame). The major difference (solid line) corresponds to the two extreme orientations ( $\epsilon || a$ ) and ( $\epsilon || c^*$ ).

synchrotron orbit, thus it corresponds to a vertical orientation of the **b**-axis), the  $a_\theta$  coefficient varies between 0 and 0.85, values that correspond to two experimental signals  $I_a$  and  $I_{c^*}$  containing only  $I_{\text{heme}}$  when  $\epsilon || a$  or  $(0.85I_{\text{normal}} + 0.15I_{\text{heme}})$  when  $\epsilon || c^*$ , respectively. The pure  $I_{\text{normal}}$  component is then recovered as  $I_{\text{normal}} = (I_{c^*} - 0.15I_a)/0.85$ ; the  $I_{\text{normal}}$  component is extremely sensitive to the type and binding geometry of the heme axial ligand, providing the fine structural details of the coordination of various molecules to the Fe-heme, like proximal histidine, CN, CO, NO, and  $H_2O$ .

In Figure 3, upper frame, XANES spectra collected at conveniently chosen angles in the plane of the **ac**\* crystal axes of a MbCN protein crystal are shown. In the lower frame, their differential spectra display the same shape with different intensity, according to the above-mentioned XANES dichroism. The two components  $I_{\text{heme}}$  and  $I_{\text{normal}}$  of the dichroic signal are derived from these angular-dependent spectra.<sup>15</sup>

Treatment of XANES spectra has been performed using the MXAN procedure.<sup>16</sup> It works in the standard multiple scattering (MS) theoretical environment using the muffin-tin (MT) approximation for the shape of the potential and the so-called “extended continuum” scheme to calculate both the bound states and the continuum part of the XAS spectrum. The overcoming of the MT approximation<sup>17,18</sup> and the use of a self-consistent (SCF) procedure<sup>19</sup> for the whole cluster to generate the potential is the way to remove the use of arbitrary parameters of the MT approximation and the systematic error linked to them. However, their full use in a fitting procedure is still too complex and prohibitively time-consuming. Moreover, during a fitting procedure, the calculation of a SCF charge density for a geometry

far from the “true one” could be even harmful, as it could select wrong excited electron configurations. For these reasons, in a number of previous publications on heme-proteins<sup>5,8,15</sup> we have calculated the SCF MT potential related to the starting structure, chosen on the basis of the information derived by high resolution diffraction data available in the protein data bank, but we were unable to recalculate the potential when distorting the starting structure, at each step of structural optimization. The inability to recalculate the potential was a source of a systematic error in the fitting procedure: the more the starting structure is far from the “true” one, the more this error affects the results. More recently, we have tested a different strategy, that is, the possibility to “mimic” SCF by refining some MT parameter linked to the potential calculation during the MXAN structural optimization.<sup>20</sup> The potential in this way can be quickly recalculated, but another source of systematic error is introduced if a relevant statistical correlation exists between the refined potential parameters and some structural parameters. By using the latter procedure, the MXAN analysis has been compared with extended X-ray absorption fine structure (EXAFS) when applied to several model systems, from hydrated ions to crystals,<sup>21–24</sup> and the numerical results were in fine agreement; heme models and hemeproteins are more challenging to the MT theory due to the strong asymmetry of their structure around the Fe ion. However, we showed<sup>20</sup> that the overall accuracy of MXAN in solution, including the related systematic errors, is approximately comparable to that of 1.4 Å resolution X-ray diffraction (XRD) on crystals.

The second example is that of murine neuroglobin.<sup>25,26</sup> This monomeric protein is arranged in the orthorhombic R32 space group. The unit cell contains 18 protein monomers, and the corresponding heme groups are shown in Figure 2 right frame, in the case of the carbonmonoxy-derivative (PDB code 1W92). The molecules of the prosthetic group are still oriented approximately parallel or antiparallel to each other, and the heme normals are very close to the **c**-axis:  $a_\theta = c = 0.95$  along this direction. By rotating the crystal around the **a**-axis or the **b**-axis it corresponds to a variation of  $a_\theta$  between 0.024 and 0.95, so that the extraction of the pure  $I_{\text{normal}}$  component is more favorable than in the  $P2_1$  crystal of myoglobin, in a beamline equipped for orienting the crystal along a specific crystal axis.

The feasibility of a structural study combining polarized XAS and XRD studies on the same protein crystals has already been demonstrated.<sup>27</sup> Polarized XANES on single crystals have been proved to be a valuable tool to elucidate at atomic resolution the local structure of the metal site under investigation.<sup>15,28</sup> Polarized spectra can directly provide the axial ligand coordination by suppressing the  $I_{\text{heme}}$  contribution, whose major intensity is predominant in solution.<sup>4,20</sup> Working at a MAD beamline equipped for this specific purpose, namely, beamline 10.1 at SRS (Daresbury, UK),<sup>29</sup> it has been possible to determine both the 1.4 Å X-ray structure of the ferric cyanomet derivative of sperm whale Mb (MbCN) and, by XANES, the local structure around the Fe ion with enhanced resolution,<sup>15</sup> comparable to that of atomic resolution XRD.

Applications of the XANES spectroscopy to single crystals of sperm whale Mb derivatives, and NgbCO, are reported and compared with results of XRD determinations. In the case of NgbCO, the parallel determination by XAS in solution is also reported. The potentials and limitations of XANES spectroscopy and the MXAN method on the subject of pursuing a XRD/XAS joint analysis are discussed.



TABLE 1: XANES Structural Determinations from Single Crystals<sup>a</sup>

sample	data analysis technique	Fe–Np (Å)	Fe–His (Å)	Fe–XY (Å)	tilting (deg)	bend (deg)	X–Y (Å)
MbCN	XANES (SCF-fixed)	2.01(2)	2.07(2)	1.87(2)	-	10(7)	1.10(2)
	XANES (optim)	1.98(3)	2.13(3)	1.92(3)	4(4)	4(3)	1.21(1)
	average	1.99(2)	2.10(2)	1.89(2)	-	7(4)	1.15(5)
	XRD 1.4 Å <sup>15</sup>	2.04	2.08	1.92	7	13	1.11
MbCO	XANES (SCF-fixed)	2.00(2)	2.06(3)	1.83(2)	-	14(4)	1.07
	XANES (optim)	1.97(2)	2.07(3)	1.90(2)	3	15	1.20(2)
	average	1.98(1)	2.06(2)	1.86(3)		16(2)	1.13(7)
	XRD 1.1 Å <sup>38</sup>	1.98	2.06	1.73	4	7	1.12
		1.98	2.06	1.82	9	9	1.09
	XRD 1.1 Å <sup>37</sup>	2.02	2.08	1.90–1.84	4; 5	13; 15	1.15; 1.17
MbNO	XANES (SCF-fixed)	2.02(2)	2.11(2)	1.92(2)	-	88(3)	1.10(3)
	XANES (optim)	2.00(2)	2.16(2)	1.94(2)	-	36(5)	1.17(4)
	average	2.01(3)	2.13(3)	1.93(2)	-	61(27)	1.13(4)
	XRD 1.7 Å <sup>42</sup>	2.08	2.18	1.89	-	68	1.15
	XRD 1.3 Å <sup>43</sup>	2.05	2.08	1.87	-	36	1.20
Mb•CO	XANES (SCF-fixed)	2.03(2)	2.05(2)	3.08(7) <sup>c</sup>	37(7)	31(5)	1.24
	XANES (optim)	2.00(2)	2.00(2)	3.23(4)	19(7)	37(17)	1.13
	average	2.01(1)	2.02(3)	3.15(8)	28(9)	35(5)	1.18(6)
	XRD 1.7 Å <sup>49</sup>	2.00	2.11	2.84	23	45	1.21
	XRD 1.5 Å <sup>50</sup>	1.97	2.25	3.60	27	54	1.12
deoxy-Mb	XANES (SCF-fixed)	2.05(3)	2.10(2)	3.5(1) <sup>c</sup>			
	XANES (optim)	2.04(6)	2.06(3)	3.2(1)			
	average	2.04(3)	2.08(2)	3.3(2)			
	XRD 1.15 Å <sup>37</sup>	2.07	2.14	3.5			

<sup>a</sup> The d(Fe–Np) distance is derived from the  $I_{\text{heme}}$  spectrum. All of the other parameters are derived from the  $I_{\text{normal}}$  spectrum. Numbers in parentheses represent the statistical error or the maximum semidispersion error (italic) on the last digit. In some cases the parameter of tilting and X–Y distance has been refined in the first optimization cycle and then kept constant before the last loop of minimization and error analysis. <sup>b</sup> Two conformers were found for the CO binding geometry. <sup>c</sup> In the Mb•CO adduct, the CO molecule is present in the first docking site, while a water molecule at about 3 Å is fitted for the deoxy-Mb species.

## Materials and Methods

**Protein Purification and Crystallization.** The synthetic gene coding for murine Ngb (mutant C55S/C120S) was cloned in the pet14b vector and expressed as N-terminal His6-tagged protein in *Escherichia coli* strain BL21(DE3)pLysS. Protein expression and purification has been detailed elsewhere,<sup>30</sup> and for the aim of this paper we report only the details of the crystallization procedure. Crystals grew in a 1:1 mixture of protein (10 mg/mL) and reservoir solution (1.6 M ammonium sulfate, 0.1 M MES, pH 6.5, 10% v/v dioxane), at 20 °C in the hanging-drop method, and their size was about 100 × 100 × 150 μm. To prepare ferrous CO bound form, crystals were transferred into a suitable glass slide filled with mother liquor saturated with CO which contained 25% glycerol (as cryoprotectant) and 4 mM sodium dithionite. Reduced CO bound crystals were frozen in liquid nitrogen and stored in a dewar.

**Data Collection.** The polarized XANES spectra (in fluorescence mode) and the XRD data (at 1.7 Å resolution) of protein single crystals, collected at 100 K, have been measured at Daresbury, CCLRC 10.1 beamline<sup>29</sup> and at the European Synchrotron Radiation Facility in Grenoble, ESRF-BM30-B Fame beamline<sup>31</sup> at 15 K.

Details on crystal orientation and X-ray structure determination have been previously reported (MbCO by Della Longa et al.;<sup>32</sup> MbCN by Arcovito et al.;<sup>15</sup> NgbCO by Vallone et al.<sup>25</sup>). The same single crystals were used when acquiring XANES spectra at different orientations.

X-ray doses absorbed by the crystals depend on the experimental conditions which were very different at the Daresbury and ESRF facilities, the latter emitting a much higher X-ray flux. At ESRF, according to the measured flux (10<sup>11</sup> photons/s at 7100 eV) and spot size (3 × 10<sup>4</sup> micron<sup>2</sup>), the X-ray dose absorbed by our protein crystals is approximately 600 Gy/s, and

a dose of 9 MGy is absorbed in 4 h, the time needed for a complete XRD + XANES experiment assuming to work with a fixed spot on the sample. The spot position actually changes during the experiment; however, this value is still below the maximum recommended dose to a protein crystal, that is 30 MGy.<sup>33</sup>

Cryoradiolytic effects at the level of the Fe-heme site are probed by XANES, which is highly sensitive to iron net charge and coordination symmetry. We have previously reported the water dissociation in ferric myoglobin<sup>7</sup> and CO dissociation in NgbCO at very low temperatures<sup>30</sup> as due to heavy X-ray irradiation. The experiments reported in the present paper have been done at the best experimental conditions with minimal X-ray effects, assuring a full integrity at the heme site level and reproducibility of the XANES spectra within the beam time available to users. Further detailed studies as a function of the X-ray dose deserve to be undertaken.

**Data Analysis.** XAS data have been analyzed by means of the MXAN software package<sup>16</sup> for the low energy range (XANES) and by GNXAS<sup>34,35</sup> for the solution spectrum of Ngb in the high energy range (EXAFS).

GNXAS is a well-established method for the EXAFS analysis of materials, liquids, and biological matter. In the XANES regime, two methods have been systematically applied within the MXAN package and compared for the calculation of the MT potential (namely, “SCF-fixed” and “optim.”) showing the effect on the choice of potential parameters with respect to the final results. In fact, up to date, in spite of the occasional differences found in the final values of the structural parameters, we did not find relevant differences in the residual square function of the best fits, justifying a choice between them. Therefore, we have considered these procedures as two independent methods whose accuracy is affected by its own

TABLE 2: NgbCO Structural Determination<sup>a</sup>

experiment	Fe–Np (Å)	Fe–His (Å)	Fe–CO (Å)	tilt (deg)	bend (deg)	C–O (Å)
XRD 1.7 Å <sup>25 b</sup>	2.00(15)	2.11(18)	1.81(14)	-	22	1.03(15)
XANES (SCF-fixed)	2.05(7)	2.07(3)	1.85(3)	14(17)	10(10)	1.12(3)
XANES (optim)	1.97(2)	2.06(2)	1.86(2)	10(3)	19(5)	1.23(2)
average	2.01(3)	2.06(2)	1.85(2)	12(9)	15(6)	1.17(6)
EXAFS (solution)	1.99 (1)	2.10(4)	1.81(2)	-	7(7)	1.08 (2)
XANES (solution)	2.02(2)	1.96(7)	1.86(5)	-	8(8)	1.10

<sup>a</sup> Numbers in parentheses represent the statistical error of the last digits. <sup>b</sup> Estimated standard uncertainties are calculated by using DPI<sub>free</sub>.<sup>51</sup> The standard uncertainty on the Fe–C–O angle is not quoted as it has been refined automatically based on the restraint listed in the CCP4 library.

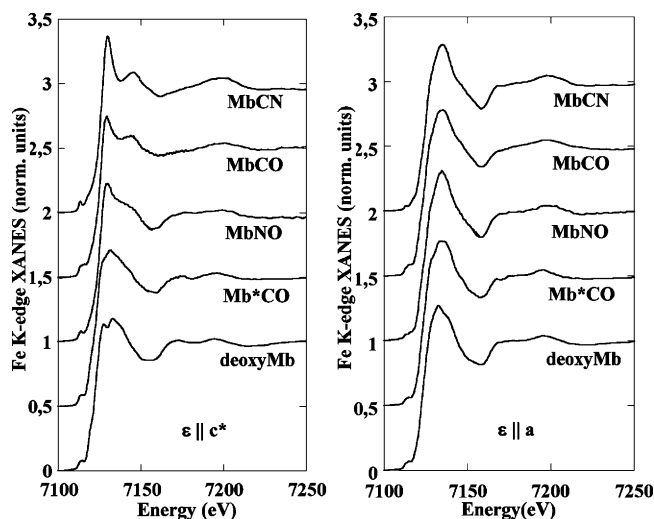


**Figure 4.** Polarized XANES spectra of different derivatives of Mb as indicated in the figure. Left frame: ( $\epsilon||c^*$ ) polarization; right frame: ( $\epsilon||a$ ) polarization. XANES fingerprints vary according to the type and binding geometry of axial ligands to the heme iron.  $I_{\text{normal}}$  and  $I_{\text{heme}}$  are obtained by linear combining the ( $\epsilon||a$ ) and ( $\epsilon||c^*$ ) polarized spectra of the  $P2_1$  crystals as described in the Introduction.

systematic errors. Values of distances and angles in Tables 1 and 2 are averaged as a last step, and their respective error is obtained from uncertainty propagation theory. Both the “SCF-fixed” procedure<sup>8,15</sup> and the “optim.” procedure<sup>20</sup> for the MT potential calculation have been described in our previous works.

The real part of the exchange term was calculated using the Hedin–Lundqvist energy-dependent potential,<sup>36</sup> while all of the inelastic losses were taken into account by convolution with a phenomenological broadening function  $\Gamma = \Gamma_c + \Gamma(E)$ . The constant part  $\Gamma_c$  includes contributions from the core-hole lifetime, while the energy-dependent term  $\Gamma(E)$  represents the inelastic processes. The experimental resolution was taken into account by a Gaussian convolution (0.6–0.8 eV) of the theoretical spectrum. The method introduces two free parameters linked to the potential, and two parameters linked to  $\Gamma(E)$ , that are derived during the fit.<sup>20</sup>

The Fe-porphyrin macrocycle, and the ligand molecules, were included in the atomic cluster used for XANES analysis. The cluster size and the  $I_{\text{max}}$  value (i.e., the maximum  $l$  value of the spherical harmonic expansion of the scattering path operators) were chosen on the basis of a convergence criterion.

## Results and Discussion

**Polarized XANES of Hemeproteins.** The polarized XANES values of hemeproteins strongly depend on the presence and the type of the sixth ligand coordination. Figure 4, left frame, clearly shows the changes of ( $\epsilon||c^*$ ) polarized XANES spectra (mainly contributed by the  $I_{\text{normal}}$  component) displayed along

various crystals of sperm whale Mb (CN, CO, NO, low temperature CO photoproduct, deoxy) having all  $P2_1$  symmetry. Spectra are sensitive to the iron sixth ligand atom (e.g., CO vs NO) and even to the more distant atom of small molecules (e.g., CO vs CN); in a previous work<sup>23</sup> on hexacyanoferrat(II) and (III) in solution we showed that, contrary to EXAFS, the XANES signal can directly probe the chemical nature of the metal ligands, and not only their binding geometry.

Weaker modifications affect the ( $\epsilon||a$ ) polarized spectra ( $I_{\text{heme}}$  component, right panel of Figure 4) as, in spite of their large number, heme-plane structural parameters are highly restrained due to the rigidity of the porphyrin ring. Indeed, this is the reason why even solution spectra are diagnostic of the axial coordination in hemeproteins, as in these systems the  $I_{\text{heme}}$  contribution can be considered a rather constant “background signal”.

Whereas the XANES fingerprints probe the axial coordination, their fine structure provides the metrics via the full MS analysis. Figure 5 shows how the MXAN procedure (see Methods) can be applied to interpret the Fe K-edge XAS spectrum, extract the ligand binding geometry, and provide heme structural parameters. XANES features emerge as single scattering (SS) or MS contributions from a cluster of about 32 atoms around the Fe atom. It is possible to calculate the theoretical  $I_{\text{normal}}$  and  $I_{\text{heme}}$  spectra of MbCO as a function of the cluster size (panel A and B of Figure 5, respectively; here the “optim.” procedure to build the MT potential is used). It is necessary to include all of the porphyrin macrocycle, the proximal histidine, and the sixth ligand to reproduce the experimental spectra of MbCO single crystal. As stated in the Materials and Methods Section, the comparison between theory and experiment is done after convoluting the theoretical spectra with an energy-dependent broadening function. In panel C and D the theoretical  $I_{\text{normal}}$  and  $I_{\text{heme}}$  spectra are still reported before convolution (dotted spectra) and after convolution (solid line). The resulting spectra fit the experimental ones of the MbCO crystal (circles), after optimization of the structural parameters of the atomic cluster. It is evident from inspection of the spectra in panel C and D, that all of the features from the rising edge up to about 200 eV above the edge are well reproduced by the one-electron MS theory using a MT potential (features 1–6 of the  $I_{\text{normal}}$  spectrum and features 1–7 of the  $I_{\text{heme}}$  spectrum). In particular, we note that peaks 1–3 of the  $I_{\text{normal}}$  spectrum emerge beyond the first shell calculation as MS features of the axial pathways including the second and third shell and are strongly sensitive to the ligand binding geometry, whereas features 2 and 3 of the  $I_{\text{heme}}$  spectrum emerge as 3-shell contributions and are sensitive to the overall structure and distortions of the porphyrin macrocycle.

In Figure 6 the MXAN fits (solid lines) carried out on the  $I_{\text{normal}}$  spectra of MbCN, MbCO, MbNO, Mb\*CO, and deoxy-Mb (circles) are displayed. The one-electron MS analysis, in

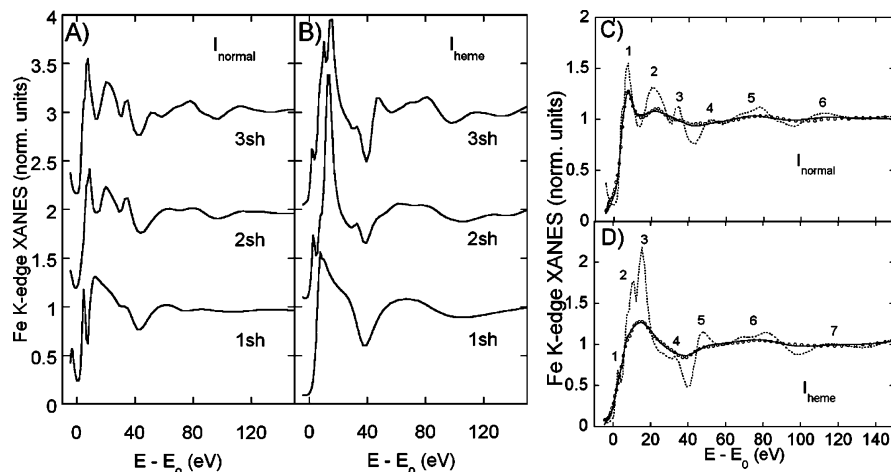


**Figure 5.** (A and B) XANES calculation (without broadening factors) of the  $I_{\text{normal}}$  and  $I_{\text{heme}}$  components of MbCO as a function of the cluster size. A final size of 32 atoms including the whole porphyrin ring, the CO molecule, and the proximal histidine residue are necessary to reproduce the experimental spectra. (C and D) MXAN fits (solid line: with broadening; dotted line: without broadening) of the experimentally determined  $I_{\text{normal}}$  and  $I_{\text{heme}}$  components (circles).

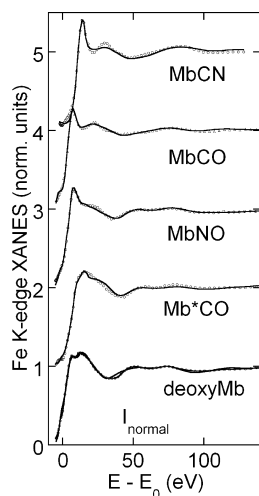


**Figure 6.** MXAN fits (solid line) of the  $I_{\text{normal}}$  component (dots) of the Mb derivatives of Figure 4. The MXAN fits shown here have been performed by using the “optim” method. The “SCF-fixed” method produces very similar results, undistinguishable by visual inspection.

the frame of the MT approximation, provides a good simulation of both hexa-coordinate and five-coordinate derivatives of myoglobin. The structural results obtained by the fitting procedure applied to  $I_{\text{normal}}$  (for the axial parameters) and  $I_{\text{heme}}$  (for the Fe–N<sub>p</sub> distance) are summarized in Table 1 and compared with structural parameters from XRD. Both of the results obtained by using the “SCF-fixed” and the “optim” methods to calculate the potential are reported.

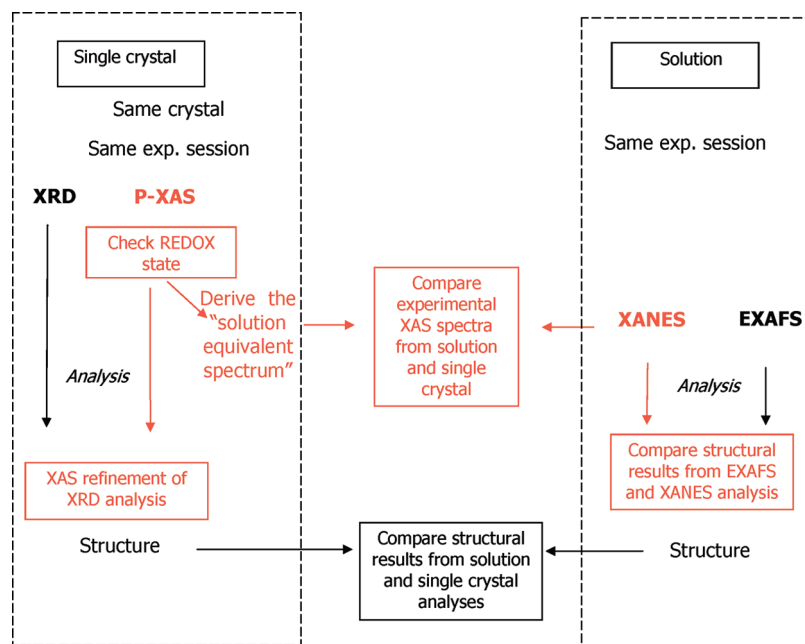
As far as it concerns the first shell distances, the two methods (“optim” and “SCF-fixed”) provide values in very good agreement with each other (the maximum discrepancy being 0.03 Å out of errors). Relative to the XRD determinations, our results are consistent with high (1.1 Å) resolution crystal structures, that is, MbCO and deoxyMb. In the case of MbCO, as previously reported,<sup>8</sup> our data support the results by Vojtechovsky et al.<sup>37</sup> rather than those by Kachalova et al.<sup>38</sup> This last determination is more consistent with heme model systems<sup>39</sup> and related DFT calculations,<sup>40</sup> including a ~0.1 Å decrease of the Fe–C distance; however, a recent XRD study on MbCO at 1.21 Å resolution (PDB code 3E4N)<sup>41</sup> still confirms the structure with a longer Fe–C distance (in both of the two conformers found), in agreement with our data. In the other cases, the XRD

resolution is lower as well as the accuracy on these parameters, and the XAS values become important restraining factors to enhance resolution at the metal site, as we demonstrated for MbCN.<sup>15</sup>

The determination of the bending angle of the ligands, CO, CN, and NO, depends on weaker signals associated to second and third shell MS pathways and is very accurate in the case of MbCO and MbCN but becomes less accurate in the case of MbNO; actually, the higher the intensity and phasing (“focusing effect”) of the signals related to the Fe–X–Y geometry, the higher the accuracy is in its determination by XAS.

In spite of their relatively small statistical errors, discrepant values of the C–O and C–N distances (0.1 Å out of errors), and of the Fe–N–O bending angle (40° out of errors), occur by using the two different methods to calculate the MT potential. This fact highlights the existence of systematic errors related to the MT potential calculation that cannot be neglected. As explained in the Material and Methods Section, we have reported in Table 1 results from the two procedures as independent measuring methods whose accuracy is affected by its own systematic errors; therefore, the average of the two determinations (distances and angles) is displayed in the same table, its error being obtained from uncertainty propagation theory. Following this assumption, the agreement between XAS and high resolution XRD is extended to all of the structural parameters of the metal site, including the bond length of the bound diatomic molecules. Moreover, a more reliable evaluation of parameters like the bending angle in MbNO (61 ± 27)° is obtained using the maximum semidispersion error, for X-ray structures known at lower resolution. Our results on MbNO confirm the XRD determination reported in literature<sup>42,43</sup> that are known to be in contrast with solution EXAFS measurements.<sup>44</sup> However, many environmental parameters (preparative method, pH, temperature) have been suggested to affect the chemical and structural state of this derivative at the level of the iron site<sup>43</sup> and can be responsible of this discrepancy. This topic is currently part of our work-in-progress activity and will be specifically addressed, using the protocol described in Scheme 1, in future studies.

In Figure 7 the XRD map (lower frame) and the Fe K-edge XAS analysis (upper frame) of murine NgbCO are displayed. According to Scheme 1, the XAS measurements have been carried out on both the R32 single crystal opportunely oriented

SCHEME 1: Proposed Method To Determine Metal Site Structure in Proteins<sup>a</sup>

<sup>a</sup> Experimental design of a combined XRD-XAS measurement. XANES can improve the reliability of both XRD (single crystal) and EXAFS (solution) analyses, providing a validation of the results and a cross-check for the comparison of the two techniques when both data are available on a given metal site.

and in solution. As mentioned in the Methods Section, the *R*32 crystal of NgbCO shows a very strong XAS angular dichroism, making easy to extract the  $I_{\text{heme}}$  and  $I_{\text{normal}}$  components from the experimental XANES spectra collected at various angles. The two components are depicted in panels A and B of Figure 7, upper frame (panel A is a blow-up of the pre-edge region). The 2:1 weighted average of the two components and the solution XANES spectrum are also displayed for visual comparison. The comparison was required since at room temperature crystals of reduced Ngb tend to crack following CO soaking, and the X-ray structure of NgbCO (PDB code 1W92), obtained by flash freezing the soaked crystal, was found to undergo a substantial conformational change compared to the one of the ferric form (PDB code 1Q1F), involving a sliding motion of the heme falling into the proximal cavity. Thus, since cracking upon CO binding at room temperature suggests a further relaxation, a crystal packing constraint at the Fe-heme site level could not be excluded. Independently from the systematic errors linked to the XAS analysis, the high similarity between the two experimental XANES spectra (crystal and solution) gives the best direct evidence that the crystal preparation protocol does not induce relevant constraints at least at the level of the Fe-heme structure of NgbCO.

In Figure 7, upper frame panels C and D, the  $I_{\text{heme}}$  and  $I_{\text{normal}}$  XANES spectra collected onto the *R*32 crystal of NgbCO are reported (open circles), together with the best fitting spectra (solid line) found using the MXAN package. Finally, in panel E, the Fourier transform of the EXAFS solution spectrum of NgbCO (dots) and the best fit obtained via the GNXAS package (solid line) are reported. The XAS analysis in solution (both EXAFS and XANES) has been previously carried out,<sup>30</sup> and the EXAFS analysis is shown in the figure only to completely address the protocol reported in Scheme 1. The relevant structural parameters obtained by the combination of all of these measurements are displayed in Table 2 and compared with results from 1.7 Å resolution XRD. As well as for myoglobin, only the Fe–N<sub>p</sub> distance is obtained from the analysis of  $I_{\text{heme}}$ ,

whereas the axial parameters are derived from  $I_{\text{normal}}$ . As the experimental  $I_{\text{heme}}$  spectrum of NgbCO is available only up to 120 eV beyond the edge, the MXAN analysis of this spectrum is carried out on a shorter energy range as compared to all of the other experimental spectra, that are analyzed up to about 200 eV beyond the edge. As a consequence, a lower accuracy on the Fe–N<sub>p</sub> distance is obtained: 2.05(7) Å by using the “SCF-fixed” method, and 1.97(2) Å by using the “optim” one. The average of the results from the two methods gives a better agreement with the independent determinations by XRD and EXAFS in solution; however, the importance of choosing a large energy interval for the XANES analysis via the MXAN package is confirmed.

The numerical results obtained from the MXAN analysis for the axial parameters of NgbCO and MbCO are almost identical, due to the similarity between the two experimental  $I_{\text{normal}}$  spectra (see Figures 6 and 7c). Residual differences are observable (e.g., the intensity of the main peak of the  $I_{\text{normal}}$  component is enhanced in NgbCO with respect to MbCO); however, they are accounted for by MXAN package using different broadening parameters within a very similar structure. As explained above, the broadening function used here is phenomenological and cannot give reliable clues on the physical origin of such spectral changes. Electronic damping and conformational disorder can affect the low photoelectron energies,<sup>45</sup> but none of them is treated here quantitatively. Theoretical improvements of the imaginary part of the complex potential used,<sup>45</sup> and molecular dynamics<sup>20</sup> should be implemented in the MXAN code to give a more exhaustive approach to this problem.

Last, it is worth noting that, given an exact orientation of the crystal and the crystallographic structure, the XANES spectrum can be calculated independently from C4 symmetry approximation. For this purpose, the  $a_\theta$  and  $b_\theta$  values from eq 3 are not used, and the calculation has to be repeated for any asymmetric unit and finally averaged. This analysis becomes heavily time-consuming; for instance, in the fitting procedure of NgbCO,



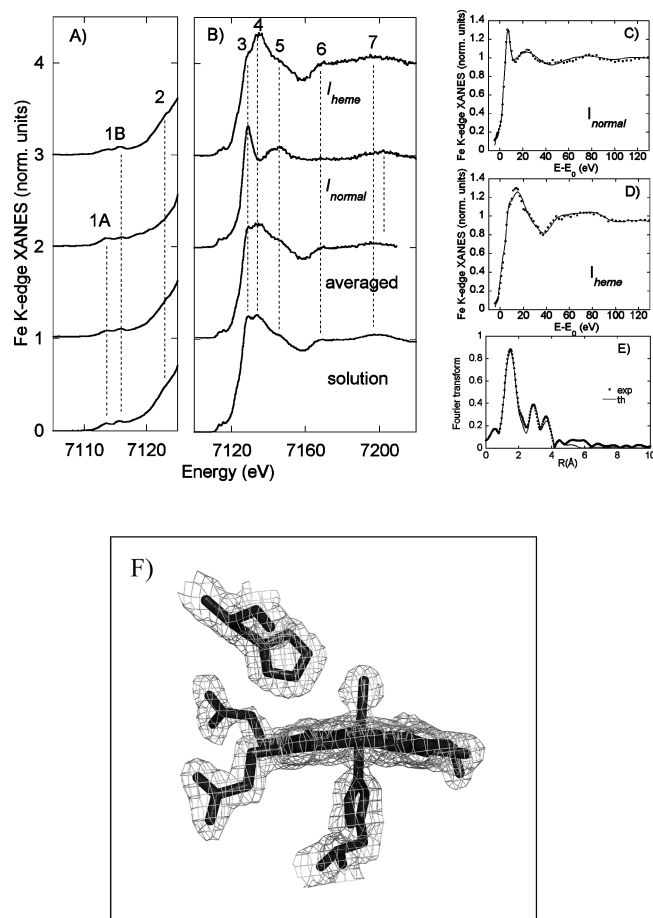


**Figure 7.** Panels A and B: pre-edge and Fe K-edge XANES spectra of murine NgbCO. From top to bottom:  $I_{\text{heme}}$  and  $I_{\text{normal}}$ ; their weighted average giving the “solution equivalent” spectrum and the experimental solution XANES spectrum. Eight labeled features (1A, 1B, 2–7) are discernible in all spectra. Panels C and D: MXAN best fits (solid lines) of  $I_{\text{normal}}$  and  $I_{\text{heme}}$  (open circles). Panel E: Fourier transform of the EXAFS spectrum in solution (dots) and best fit obtained by the GNXAS procedure (solid line). Panel F: blow-up of the electron density map of the active site of NgbCO, including the proximal (H96) and distal (H64) histidines; the density is contoured at  $1\sigma$ .

the spectrum has to be calculated 18 times at each optimization step, and the overall fitting procedure becomes 18 times longer.

To assess the adequacy of the C4 approximation, the extraction of the absorption tensor described in eq 1 from the experimental data is required. This procedure has been performed on a  $P2_1$  Mb sample (data not shown). For this space group, the absorption tensor contains four independent elements,  $\sigma_x$ ,  $\sigma_y$ ,  $\sigma_z$ , and  $\sigma_{xz}$ , which are functions of X-ray energy at the Fe K edge. Under the C4 symmetry,  $\sigma_x = \sigma_y$  and  $\sigma_{xz} = 0$ . According to the extracted values of the tensor, both  $(\sigma_x - \sigma_y)$  and  $\sigma_{xz}$  functions are negligible, that is, their related signal is within 1% of the absorption jump, with only a 3% bump at 7120 eV.

**Ngb Analysis.** In the case of Ngb the combination of XANES and XRD gives new insights of the functional transition of the protein upon ligand binding. According to MD simulations, the heme sliding distributions along its first essential eigenvector in the crystal and in solution<sup>46,47</sup> are different at room temperature for NgbCO. In solution, the conformational distribution is peaked around a position close to the crystallographic structure of deoxy-Ngb (i.e., with no heme sliding and a major steric hindrance between CO and distal histidine). In the crystal the MD simulation at room temperature shows a double-peaked

distribution. A first, higher maximum is around a position close to the crystallographic structure of NgbCO, with sliding of the heme and no steric hindrance between the CO molecule and the distal histidine. A second, lower one, is located near that of deoxy-Ngb. However, in the cryo-trapped crystal, only the first conformation is observed by XRD as significantly populated. Accordingly, in our XAS experiments in solution, at cryogenic temperature, the entire conformational ensemble, centered around the deoxy-like one (with no heme sliding), should be probed. Conversely in the crystal, only the more populated conformation, visualized by XRD (with sliding of the heme) should contribute to the measured XAS spectra. In spite of the large rearrangement of the protein environment and of the heme location predicted by MD, the local structure around the Fe ion in NgbCO determined by XAS seems unaltered between the crystal and the solution sample. As a consequence, no residual energy should be stored here as due to crystal packing, to be delivered with cracking at room temperature. This result reinforces the model proposed to explain the functional transition of the protein when an exogenous ligand replaces the distal histidine in the sixth position. The residual energy involved in the protein relaxation responsible of cracking the crystal does not reside in the heme pocket but is rapidly transferred at peripheral sites of the protein (more likely the CD corner) so that the final tertiary rearrangement of the protein in solution can be reached.

**Instrumentation Development.** The presence of beamlines at synchrotron facilities, where the combination of experiments in crystal and solution using XAS and XRD is available, could be a valuable tool to deeply investigate a large class of proteins such as those containing metal centers. As stated above, the structural resolution obtained by XANES data in solution is comparable with 1.4 Å resolved X-ray data and converges in single crystals to a higher resolution level<sup>15</sup> as a function of the relative orientation of the symmetry-related molecules. A diagram showing the rationale of applying XAS to both single crystal and solution samples of metalloproteins is sketched (Scheme 1). The potential advances in knowledge derived from such an approach are depicted in red: XAS of polarized spectra can be used to probe the redox state and to refine the active site structure determined by XRD.<sup>15,28</sup> Similarly, the XANES and EXAFS analyses can be jointly performed in solution and their results compared to each other.<sup>20,30</sup> Lastly and more importantly, the “solution equivalent spectrum” can be obtained by a weighted sum of polarized spectra of the crystal, so that the single crystal and solution states can be directly compared to test if the crystallization procedure has selected a particular protein substate.<sup>7</sup> In this framework, hemeproteins constitute a special case giving a further advantage: in fact, for these proteins the X-ray structure can be collected together with angular-dependent XAS spectra in the same crystal; moreover, XAS spectra in solution can be also acquired, and a direct and precise comparison with the crystal state is possible.

## Conclusions

The possibility to derive the widest possible number of information from the same sample is always an aim for any experimentalist. This fact is even more evident when the sample is a protein crystal. In this case the bottleneck of the structural investigation is often the crystallization production.<sup>48</sup> Moreover, these crystals are often poorly or anisotropically diffracting, leading to low resolution data. Thus, it is mandatory to obtain as much as possible from each protein crystal. Therefore, combining experimental data using XRD and XANES on protein

crystal allows us to obtain the local structure around the metal center with an increased resolution, which can provide the structural determinants associated with the affinity of an exogenous ligand such as the small diatomic gaseous molecules CO, CN, and NO. Moreover, XANES spectra can be also acquired in solution; thus, any crystal constrain onto the local structure around the metal can be tested. Finally, the intrinsic dichroism of the heme, when irradiated by the polarized synchrotron X-rays, is a property that allows increasing the structural resolution obtained applying the MXAN package to polarized XANES spectra from the crystal, with respect to the same analysis onto the solution spectrum of the protein.

**Acknowledgment.** Thanks are due to the European Synchrotron Radiation Facility and to STFC Daresbury Laboratory for provision of synchrotron radiation facilities and to CASPUR, with the standard HPC grant 2009 entitled “A Combined X-ray Absorption Spectroscopy, Molecular Dynamics Simulation and Quantum Mechanics Calculation procedure for the structural characterization of ill-defined systems”. A.A. is grateful for the financial support by the Italian Ministry of University and Research (MiUR) [Linea D1 “ex-60%” 2007-2008, “Emoproteine di interesse Biomedico”, Università Cattolica Sacro Cuore], and B.V. is grateful for the financial support by MiUR of Italy grants FIRB RBLA03B3KC\_004 and PRIN 20074TJ3ZB\_005. M.C. is especially grateful to European Molecular Biology Laboratory (EMBL) for the financial support.

## References and Notes

- (1) Weigelt, J. *Exp. Cell. Res.* **2010**, *316*, 1332–1338.
- (2) Cook, J. D.; Penner-Hahn, J. E.; Stemmler, T. L. *Methods Cell Biol.* **2008**, *90*, 199–216.
- (3) Strange, R. W.; Feiters, M. C. *Curr. Opin. Struct. Biol.* **2008**, *18*, 609–16.
- (4) Arcovito, A.; Bonamore, A.; Hazemann, J. L.; Boffi, A.; D'Angelo, P. *Biophys. Chem.* **2009**, *147*, 1–7.
- (5) Arcovito, A.; Lamb, D. C.; Nienhaus, G. U.; Hazemann, J. L.; Benfatto, M.; Della Longa, S. *Biophys. J.* **2005**, *88*, 2954–64.
- (6) D'Angelo, P.; Lucarelli, D.; della Longa, S.; Benfatto, M.; Hazemann, J. L.; Feis, A.; Smulevich, G.; Ilari, A.; Bonamore, A.; Boffi, A. *Biophys. J.* **2004**, *86*, 3882–92.
- (7) Della Longa, S.; Arcovito, A.; Benfatto, M.; Congiu-Castellano, A.; Girasole, M.; Hazemann, J. L.; Lo Bosco, A. *Biophys. J.* **2003**, *85*, 549–58.
- (8) Della Longa, S.; Arcovito, A.; Girasole, M.; Hazemann, J. L.; Benfatto, M. *Phys. Rev. Lett.* **2001**, *87*, 155501.
- (9) Green, M. T.; Dawson, J. H.; Gray, H. B. *Science* **2004**, *304*, 1653–6.
- (10) Brunori, M. *Protein Sci.* **2009**, *19*, 195–201.
- (11) Burmester, T.; Weich, B.; Reinhardt, S.; Hankeln, T. *Nature* **2000**, *407*, 520–3.
- (12) Sun, Y.; Jin, K.; Mao, X. O.; Zhu, Y.; Greenberg, D. A. *Proc. Natl. Acad. Sci. U.S.A.* **2001**, *98*, 15306–11.
- (13) Yano, J.; Yachandra, V. K. *Photosynth. Res.* **2009**, *102*, 241–254.
- (14) Bricogne, G.; Capelli, S. C.; Evans, G.; Mitschler, A.; Pattison, P.; Roversi, P.; Schiltz, M. *J. Appl. Crystallogr.* **2004**, *38*, 168–72.
- (15) Arcovito, A.; Benfatto, M.; Cianci, M.; Hasnain, S. S.; Nienhaus, K.; Nienhaus, G. U.; Savino, C.; Strange, R. W.; Vallone, B.; Della Longa, S. *Proc. Natl. Acad. Sci. U.S.A.* **2007**, *104*, 6211–6.
- (16) Benfatto, M.; Della Longa, S. *J. Synchrotron Radiat.* **2001**, *8*, 1087–94.
- (17) Cabaret, D.; Joly, Y.; Renevier, H.; Natoli, C. R. *J. Synchrotron Radiat.* **1999**, *6*, 258–60.
- (18) Joly, Y. *Phys. Rev. B* **2001**, *63*, 125120–9.
- (19) Ankudinov, A. L.; Ravel, B.; Rehr, J. J.; Conradson, S. D. *Phys. Rev. B* **1998**, *58*, 7565–76.
- (20) D'Angelo, P.; Lapi, A.; Migliorati, V.; Arcovito, A.; Benfatto, M.; Roscioni, O. M.; Meyer-Klaucke, W.; Della-Longa, S. *Inorg. Chem.* **2008**, *47*, 9905–18.
- (21) Benfatto, M.; D'Angelo, P.; Della Longa, S.; Pavel, N. V. *Phys. Rev. B* **2002**, *65* (174205), 1–5.
- (22) D'Angelo, P.; Benfatto, M.; Della Longa, S.; Pavel, N. V. *Phys. Rev. B* **2002**, *66* (064209), 1–7.
- (23) Hayakawa, K.; Hatada, K.; D'Angelo, P.; Della Longa, S.; Natoli, C. R.; Benfatto, M. *J. Am. Chem. Soc.* **2004**, *126*, 15618–23.
- (24) Giorgetti, M.; Della Longa, S.; Benfatto, M. *J. Phys.: Conf. Ser.* **2009**, *190*, 012145–1/6.
- (25) Vallone, B.; Nienhaus, K.; Matthes, A.; Brunori, M.; Nienhaus, G. U. *Proc. Natl. Acad. Sci. U.S.A.* **2004**, *101*, 17351–6.
- (26) Vallone, B.; Nienhaus, K.; Brunori, M.; Nienhaus, G. U. *Proteins* **2004**, *56*, 85–92.
- (27) Strange, R. W.; Hasnain, S. S. Combined Use of XAFS and Crystallography for Studying Protein-Ligand Interactions in Metalloproteins. In *Protein-Ligand Interactions: Methods and Applications*; Nienhaus, G. U., Ed.; Humana Press Inc.: Totowa, NJ, 2005; Vol. 305, pp 167–96.
- (28) Yano, J.; Kern, J.; Sauer, K.; Latimer, M. J.; Pushkar, Y.; Biesiadka, J.; Loll, B.; Saenger, W.; Messinger, J.; Zouni, A.; Yachandra, V. K. *Science* **2006**, *314*, 821–5.
- (29) Cianci, M.; Antonyuk, S.; Bliss, N.; Bailey, M. W.; Buffey, S. G.; Cheung, K. C.; Clarke, J. A.; Derbyshire, G. E.; Ellis, M. J.; Enderby, M. J.; Grant, A. F.; Holbourn, M. P.; Laundy, D.; Nave, C.; Ryder, R.; Stephenson, P.; Helliwell, J. R.; Hasnain, S. S. *J. Synchrotron Radiat.* **2005**, *12*, 455–66.
- (30) Arcovito, A.; Moschetti, T.; D'Angelo, P.; Mancini, G.; Vallone, B.; Brunori, M.; Della Longa, S. *Arch. Biochem. Biophys.* **2008**, *475*, 7–13.
- (31) Proux, O.; Biquard, X.; Lahera, E.; Menthonnex, J. J.; Prat, A.; Ulrich, O.; Soldo, Y.; Trévisson, P.; Kapoujyan, G.; Perroux, G.; Taunier, P.; Grand, D.; Jeantet, P.; Deleglise, M.; Roux, J. P.; Hazemann, J. L. *Phys. Scr.* **2005**, *115*, 970–3.
- (32) Della Longa, S.; Arcovito, A.; Vallone, B.; Castellano, A. C.; Kahn, R.; Vicat, J.; Soldo, Y.; Hazemann, J. L. *J. Synchrotron Radiat.* **1999**, *6*, 1138–47.
- (33) Owen, R. L.; Rudino-Pinera, E.; Garman, E. F. *Proc. Natl. Acad. Sci. U.S.A.* **2006**, *103*, 4912–7.
- (34) Filippini, A.; Di Cicco, A. *Phys. Rev. B: Condens. Matter* **1995**, *52*, 15135–49.
- (35) Filippini, A.; Di Cicco, A.; Natoli, C. R. *Phys. Rev. B: Condens. Matter* **1995**, *52*, 15122–34.
- (36) Hedin, L.; Lundqvist, B. I. *J. Phys. C* **1971**, *4*, 2064–75.
- (37) Vojtechovsky, J.; Chu, K.; Berendzen, J.; Sweet, R. M.; Schlichting, I. *Biophys. J.* **1999**, *77*, 2153–74.
- (38) Kachalova, G. S.; Popov, A. N.; Bartunik, H. D. *Science* **1999**, *284*, 473–6.
- (39) Kim, K.; Fetting, J.; Sessler, J. L.; Cyr, M.; Hugdahl, J.; Collman, J. P.; Ibers, J. A. *J. Am. Chem. Soc.* **1989**, *111*, 403–5.
- (40) Rovira, C.; Kunc, K.; Hutter, J.; Ballone, P.; Parrinello, M. *J. Phys. Chem. A* **1997**, *101*, 8914–25.
- (41) Tomita, A.; Sato, T.; Ichiyanagi, K.; Nozawa, S.; Ichikawa, H.; Chollet, M.; Kawai, F.; Park, S. Y.; Tsuduki, T.; Yamato, T.; Koshihara, S. Y.; Adachi, S. *Proc. Natl. Acad. Sci. U.S.A.* **2009**, *106*, 2612–6.
- (42) Brucker, E. A.; Olson, J. S.; Ikeda-Saito, M.; Phillips, G. N., Jr. *Proteins* **1998**, *30*, 352–6.
- (43) Copeland, D. M.; Soares, A. S.; West, A. H.; Richter-Addo, G. B. *J. Inorg. Biochem.* **2006**, *100*, 1413–25.
- (44) Rich, A. M.; Ellis, P. J.; Tennant, L.; Wright, P. E.; Armstrong, R. S.; Lay, P. A. *Biochemistry* **1999**, *38*, 16491–9.
- (45) Natoli, C. R.; Benfatto, M.; Della Longa, S.; Hatada, K. *J. Synchrotron Radiat.* **2003**, *10*, 26–42.
- (46) Anselmi, M.; Brunori, M.; Vallone, B.; Di Nola, A. *Biophys. J.* **2007**, *93*, 434–41.
- (47) Anselmi, M.; Brunori, M.; Vallone, B.; Di Nola, A. *Biophys. J.* **2008**, *95*, 4157–62.
- (48) Chayen, N. E.; Saridakis, E. *Nat. Methods* **2008**, *5*, 147–53.
- (49) Schlichting, I.; Berendzen, J.; Phillips, G. N. J.; Sweet, R. M. *Nature* **1994**, *371*, 808–12.
- (50) Teng, T. Y.; Srajer, V.; Moffat, K. *Nat. Struct. Biol.* **1994**, *1*, 701–5.
- (51) Cruickshank, D. W. J. *Acta Crystallogr. D* **1999**, *55*, 583–601.